Memoirs of the Faculty of Engineering, Kyushu University, Vol.71, No.1, March 2011

Particle-based Simulations of Molten Metal Flows with Solidification

by

Rida SN MAHMUDAH[*], Masahiro KUMABE[*], Takahito SUZUKI[*], Liancheng GUO[**] and Koji MORITA[†]

(Received January 27, 2011)

Abstract

The solidification behavior of molten core materials in flow channels is one of the major concerns for safety analysis of the liquid metal cooled reactors. In order to analyze its fundamental behavior, a 3D fluid dynamics code was developed using a particle-based method, known as the finite volume particle (FVP) method. Governing equations that determine the fluid movement and phase change process are solved by discretizing their gradient and Laplacian terms with the moving particles and calculated through interaction with its neighboring particles. A series of molten-metal solidification experiments using a low-melting point alloy was performed to validate the developed 3D code. A comparison between the results of simulations and experiments demonstrates that the present 3D code based on the FVP method can successfully reproduce the observed solidification process.

Keywords: Fluid dynamics code, Particle-based method, Finite volume particle (FVP) method, Molten-metal solidification

1. Introduction

Understanding the solidification behavior of molten core materials in flow channels are among the important thermal-hydraulic phenomena in core disruptive accidents (CDAs) of a liquid metal cooled reactor (LMR). In CDAs of an LMR, there is the hypothetical possibility of whole-core disassembly due to overheating caused by serious transient over power and transient under cooling accidents[1)]. These will result in increase of core temperature which will lead to other accident sequences, such as cladding melting, fuel disassembly and fuel release into coolant. It is anticipated that during CDA of LMRs molten cladding and disruptive fuel flows through subassembly channels. Due to interactions of the melt with coolant and structure, the melt undergoes solidification and penetrates along the structure wall which will cause blockages in the channel. Although the occurrence of CDA is unrealistic due to denying actuations of all multiple safety systems, it is still emphasized from the viewpoint of safety design and evaluation.

[*] Graduate Student, Department of Applied Quantum Physics and Nuclear Engineering
[**] Post-doctoral Fellow, Department of Applied Quantum Physics and Nuclear Engineering
[†] Associate Professor, Department of Applied Quantum Physics and Nuclear Engineering

Many studies of melt solidification have been conducted to understand the thermal-hydraulic phenomena in CDA of LMRs. Typical experimental studies are concerned with, for example, molten jet-coolant interactions by Kondo *et al.*[2], thermite melt injection into an annular channel by Peppler *et al.*[3], and molten-metal penetration and freezing behavior by Rahman, *et al.*[4] and Hossain *et al.*[5]. In the latter two studies[4,5], numerical simulations were also performed using a 2D Eulerian reactor safety analysis code, SIMMER-III[6,7]. Although their simulations show reasonably good agreement with observed experimental results, in general Eulerian methods are limited in reproducing local solidification processes in detail because such methods cannot capture phase changes at the interface. In addition, the particular shape of flowing melt cannot be represented by mesh methods. The present study is therefore aimed at developing a reasonable computational code that can simulate the solidification and penetration behavior of melt flows onto a metal structure.

Conventional Eulerian methods encounter difficulties in representing complex flow geometries and to directly simulate the flow regime of melt flows. Lagrangian methods represent one possible approach to overcome these problems. Several particle-based methods, which are fully Lagrangian methods, have been developed in recent years. The earliest of these is the smoothed particle hydrodynamics (SPH)[8], that was specifically developed for compressible fluid calculations in astrophysics. The others are the moving particle semi-implicit (MPS) method[9] and the finite volume particle (FVP) method[10], which can be applied to incompressible multiphase flows in complex geometries. It has been validated that these are able to simulate multiphase-flow behavior with satisfactory results, such as fragmentation of molten metal in vapor explosions[11], water dam breakage with solid particles[12], and a rising bubble in a stagnant liquid pool[13]. Unlike conventional mesh methods, these particle methods do not need to generate computational grids. The construction of interfaces between different phases is also unnecessary because each moving particle represents each phase with specific physical properties.

In this study, a 3D computational code is developed to simulate the solidification and penetration behavior of melt flows. The developed 3D computational code is based on FVP for fluid dynamics and heat and mass transfer calculations. To validate the fundamental models employed in fluid dynamics, as well as heat and mass transfer calculations, a series of solidification experiments using low-melting-point alloy was simulated using the developed 3D code.

2. Physical Models and Numerical Method

2.1 Governing Equations

The governing equations for the incompressible fluids are the Navier-Stokes equation and the continuity equation:

$$\frac{D\vec{u}}{Dt} = \frac{1}{\rho}\nabla P + \frac{1}{\rho}\nabla(\mu\nabla\cdot\vec{u}) + \frac{\vec{g}}{\rho} + \frac{\vec{f}}{\rho} \tag{1}$$

$$\nabla\cdot\vec{u} = 0 \tag{2}$$

where $\vec{u}$, P, ρ and μ are the velocity, pressure, density and dynamic viscosity, $\vec{g}$ is gravitational force, and $\vec{f}$ is other forces such as surface tension force.

The following energy equation that takes into account heat and mass transfer processes is solved:

$$\frac{D(\rho H)}{Dt} = \nabla\cdot(k\nabla T) + Q \tag{3}$$

where H is the specific internal energy, k is the thermal conductivity, T is the temperature, and Q is the heat transfer rate per unit volume. The first term of the right hand side of Eq. (3) represents the

conductive heat transfer; the second term is the heat transfer at the interface between different phases.

In the present study, the surface tension force in Eq. (1) is formulated by a model based on the free surface energy[14]. The phase-change processes are assumed to be in non-equilibrium. In the following, we describe in detail the main physical models including FVP.

2.2 FVP Method

To discretize the governing equations, we choose FVP because it has been shown to be numerically stable, especially for free surface flow simulations[15]. FVP employs the same concept as conventional finite volume methods. It is assumed that each particle occupies a certain volume. The control volume of one moving particle is a sphere in 3D simulations:

$$V = \frac{4}{3}\pi R^3 = \Delta l^3, S = 4\pi R^2 \tag{4}$$

where S, V, R and Δl are the particle surface area, the particle control volume, the radius of the particle control volume, and the initial particle distance, respectively. According to Gauss's law, the gradient and Laplacian operators acting on an arbitrary scalar function ϕ are expressed by

$$\nabla\phi = \lim_{R\to 0}\frac{1}{V}\oint_V \nabla\phi dV = \lim_{R\to 0}\frac{1}{V}\oint_S \phi\vec{n}dS \tag{5}$$

$$\nabla^2\phi = \lim_{R\to 0}\frac{1}{V}\oint_V \nabla^2\phi dV = \lim_{R\to 0}\frac{1}{V}\oint_V \nabla\phi\cdot\vec{n}dS \tag{6}$$

where $\vec{n}$ is the unit vector. As a result, in FVP the gradient and Laplacian terms can be approximated as

$$\langle\nabla\phi\rangle_i = \langle\frac{1}{V}\oint_S \phi\vec{n}dS\rangle_i = \frac{1}{V}\sum_{j\neq i}\phi_s\cdot\vec{n}_{ij}\cdot\Delta S_{ij} \tag{7}$$

$$\langle\nabla^2\phi\rangle_i = \langle\frac{1}{V}\oint_S \nabla\phi\cdot\vec{n}dS\rangle_i = \frac{1}{V}\sum_{j\neq i}\left(\frac{\phi_j-\phi_i}{|\vec{r}_{ij}|}\right)\cdot\Delta S_{ij} \tag{8}$$

where $\langle\phi\rangle_i$ is the approximation of ϕ with respect to particle i and $|\vec{r}_{ij}|$ is the distance between particles i and j. The function value ϕ_s on the surface of particle i can be estimated by a linear function

$$\phi_s = \phi_i + \frac{\phi_j-\phi_i}{|\vec{r}_{ij}|}R \tag{9}$$

The unit vector of the distance between two particles, $\vec{n}_{ij}$, is expressed by

$$\vec{n}_{ij} = \frac{\vec{r}_{ij}}{|\vec{r}_{ij}|} \tag{10}$$

The interaction surface of particle i with particle j, ΔS_{ij}, can be calculated by

$$\Delta S_{ij} = \frac{\omega_{ij}}{n^0}S \tag{11}$$

where the initial number density, n^0, is defined as

$$n^0 = \sum_{j\neq i}\omega_{ij} \tag{12}$$

and the kernel function, ω_{ij}, is defined as

$$\omega_{ij} = \sin^{-1}\left(\frac{R}{|\vec{r}_{ij}|}\right) - \sin^{-1}\left(\frac{R}{r_e}\right) \tag{13}$$

where r_e is the cut-off radius and is usually chosen as $2.1\Delta l$ for the 3D systems. If the distance between two particles is larger than the cut-off radius, the kernel function is set as zero. Schematic diagram of neighboring particles around particle *i* within the cut-off radius is shown in **Fig. 1**.

Using Eqs. (9), (10) and (11), Eqs. (7) and (8) can be rearranged as

$$\langle \nabla \phi \rangle_i = \frac{S}{Vn^0} \sum_{j \neq i} \left(\phi_i + \frac{\phi_j - \phi_i}{|\vec{r}_{ij}|} R \right) \omega_{ij} \, \vec{n}_{ij} \tag{14}$$

$$\langle \nabla^2 \phi \rangle_i = \frac{S}{Vn^0} \sum_{j \neq i} \frac{\phi_j - \phi_i}{|\vec{r}_{ij}|} \omega_{ij} \tag{15}$$

Using the above gradient and Laplacian models, the governing equations can be easily discretized. These equations are then solved by the combined and unified procedure (CUP) algorithm[16], a detailed explanation of this algorithm can be found in our previous study by Guo, *et al.*[17].

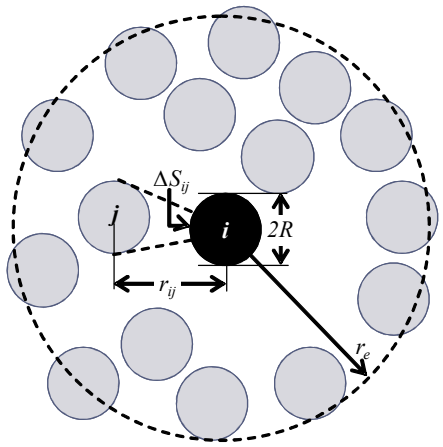

Fig. 1 Neighboring particles around particle *i* within the cut-off radius.

2.3 Heat and Mass Transfer Model

Phase change processes are based on a nonequilibrium model[18] that calculates the mass transfer occurring at the interface between solid and liquid phases. For interfaces where no phase change is predicted, only the first term on the right hand side of Eq. (3) is included. Using the Lagrangian discretization modeled by Eq. (15), it is approximated by

$$\langle \nabla \cdot (k \nabla T) \rangle_i \simeq \frac{1}{V} \sum k_{ij} \frac{T_j - T_i}{|\vec{r}_{ij}|} \Delta S_{ij} \tag{16}$$

where the thermal conductivity k_{ij} between particles *i* and *j* is defined as

$$k_{ij} = \frac{2k_i k_j}{k_i + k_j} \tag{17}$$

The thermal conductivity k_i of particle *i* is simply approximated by

$$k_i = (1 - \alpha_{l,i}) k_{s,i} + \alpha_{l,i} k_{l,i} \tag{18}$$

where $k_{s,i}$ and $k_{l,i}$ is the solid and liquid thermal conductivities of particle *i,* respectively, and $\alpha_{l,i}$ is the volume fraction of liquid phase in particle *i.*

For the interface of particle *i* where a phase change is predicted, the second term on the right hand side of Eq. (3) is calculated as

$$Q_{i,j} = a_{ij} h_i \left(T_{ij}^I - T_i \right) \tag{19}$$

where the heat transfer coefficient depends on the thermal conductivity of particle *i*:

$$h_i = 2\frac{k_i}{|\vec{r}_{ij}|} \tag{20}$$

and T_{ij}^I is defined either $T_{ij}^I = \min\left[T_{liq}, \max\left(T_{ij}^N, T_{sol}\right)\right]$ for solid-liquid interface, or $T_{ij}^I = \max\left(T_{ij}^N, T_{sol}\right)$ for solid-wall interface, where no phase change is assumed. T_{liq} and T_{sol} are the liquidus and solidus temperature, respectively; T_{ij}^N is defined as the temperature for sensible heat transfer

$$T_{ij}^N = \frac{h_i T_i + h_j T_j}{h_i + h_j} \tag{21}$$

The net heat flow rate at the interface is given by

$$Q_{i,j}^I = Q_{i,j} + Q_{j,i} \tag{22}$$

Once the net heat flow rate $Q_{i,j}^I$ is determined, the melting/freezing rate can be calculated. If $Q_{i,j}^I > 0$ and the particle *i* contains a liquid phase, it will freeze partly into a solid phase; its freezing rate is calculated by

$$\Gamma_{i,\text{freezing}} = \sum_{j \neq i} \frac{Q_{ij}^I}{H_f} \tag{23}$$

where H_f is the latent heat of fusion. If $Q_{i,j}^I < 0$ and the particle *i* contains solid phase, it will partially melt into a liquid phase; its melting rate is calculated by

$$\Gamma_{i,\text{melting}} = -\sum_{j \neq i} \frac{Q_{ij}^I}{H_f} \tag{24}$$

Otherwise, only sensible heat will be exchanged between particles *i* and *j* by applying T_{ij}^N to the interface. Using Eqs. (23) and (24), the liquid and solid masses of particle *i* can be updated by

$$\begin{aligned} m_{l,i}^{n+1} &= m_{l,i}^n + \Delta t\left(\Gamma_{i,\text{melting}} - \Gamma_{i,\text{freezing}}\right) \\ m_{s,i}^{n+1} &= m_{s,i}^n + \Delta t\left(\Gamma_{i,\text{freezing}} - \Gamma_{i,\text{melting}}\right) \end{aligned} \tag{25}$$

where $m_{l,i}$ and $m_{s,i}$ are the liquid and solid masses of particle *i,* respectively, Δt is the time step size, and superscript *n* is an iterative index for the n-th time step of calculation. Equation (25) can be used to determine the volume fraction of liquid phase in particle *i,* which is necessary in evaluating its mixture thermal conductivity from Eq. (18).

2.4 Viscosity Model

In simulations of solidification, the rheological behavior has a significant influence on not only heat and mass transfer but also the dynamics during solidification. In the present study, it is considered by estimating the viscosity of the liquid phase with its compositional development. Based on our previous study[19], the viscosity model that takes into account viscosity changes due to phase changes is expressed by the following empirical approximation:

$$\mu_{app,i} = min\left(\mu_{max}, \mu exp\left[-\frac{A\left(H_i - H_{liq}\right)}{C_p}\right]\right) \tag{26}$$

where $\mu_{app,i}$ is the dynamic viscosity of particle *i* during solidification, which is in Eq. (1) instead of μ, H_{liq} is the specific enthalpy at the liquidus point and *A* is the rheology parameter with unit of K^{-1}, the value of which will be determined by comparing simulation results with experiments. To maintain the numerical stability, the upper limit value μ_{max} is defined as

$$\mu_{max} = \mu exp\left[-\frac{A\left(H_{i,\alpha=0.375} - H_{liq}\right)}{C_p}\right] \tag{27}$$

where $H_{\alpha=0.375}$ is the enthalpy at liquid volume fraction $\alpha = 0.375$[20].

3. Experimental Setup

Figure 2 shows a schematic diagram of experimental apparatus. The apparatus consists of a melt tank and a flow channel. In the experiments, we used the low-melting-point Wood's metal as the molten material.

The melt tank section consists of a pot and a plug, both made of Teflon. The pot's neck has a 4 cm length and its upper and lower inner diameters are 0.88 cm and 0.6 cm, respectively. The plug is cylindrical in shape of 20 cm length and 1.4 cm outer diameter, except at the edge of the plug that makes contact with the upper part of the pot's neck where this plug has the same diameter to prevent the leakages of the melt in the tank. Flow of the melt is enabled onto the flow channel by pulling up the plug. The pouring rate was not measured in the experiments, and hence the pouring is assumed under free fall condition. The flow channel section is an L-shaped conduction wall made of brass or copper inclined at a certain angle to enable flow along the channel. As shown in **Fig. 2**, the dimension of L-shaped wall was 20.0×3.0×0.5 cm in length, width and thickness, respectively. Relevant material properties of Wood's metal, brass and copper are listed in **Table 1**.

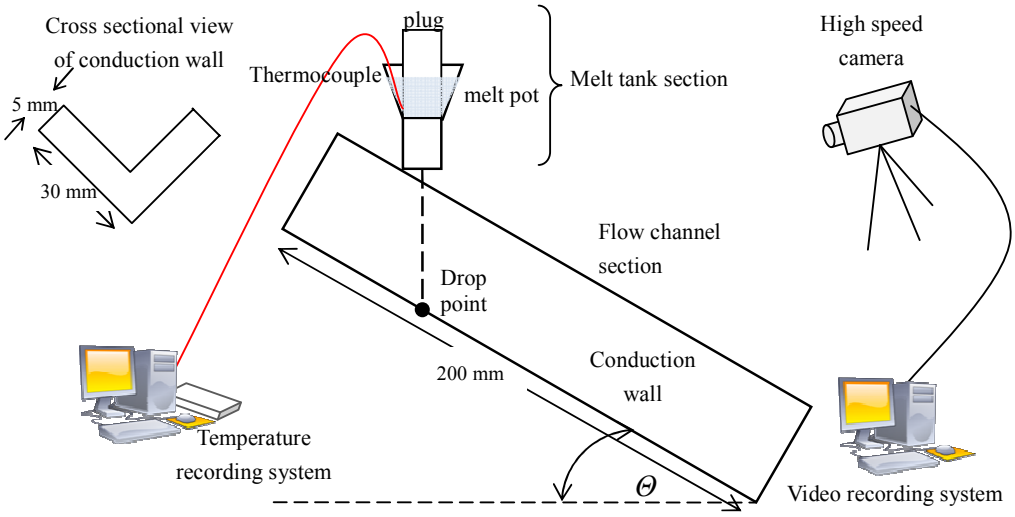

Fig 2. Experimental apparatus.

Table 1 Material properties.

Properties	Wood's Metal		Brass (solid)	Copper (solid)
	solid	liquid		
Melting point [°C]	78.8		875	1082
Latent heart of fusion [kJ/kg]	47.3		168	205
Density [kg/m^3]	8528	8528	8470	8940
Specific heat [J/kg/K]	168.5	190	377	385
Viscosity [Pa·s]	-	2.4×10^{-3}	-	-
Conductivity [W/m/K]	9.8	12.8	117	403

In preparing the experiment, the melt is heated up above the desired temperature in the range 80

– 83 °C for melt release, and then transferred to the pot. When the temperature of the melt in the pot has reach the desired temperature, the plug is extracted, and the melt is allowed to discharge from the pot onto the conduction wall. During the experiments, temperatures in the pot and at the drop point onto the conduction wall (see **Fig. 2**) are measured by thermocouples. A high-speed camera is used to record the transient behavior of the melt and to measure its penetration length along the conduction wall until the melt has completely solidifies. Solidification takes about 0.2 – 0.8 s. A series of experiments was conducted with various parameters, *i.e.* wall material and melt volume. Conditions for the solidification experiments are summarize in **Table 2**.

Table 2 Conditions of solidification experiments.

Case	A	B	C
Wall material	Copper	Brass	Copper
Initial melt temperature	81.2 °C	82.0 °C	80.4 °C
Melt volume, V_m	1 cm^3	1.5 cm^3	1.5 cm^3

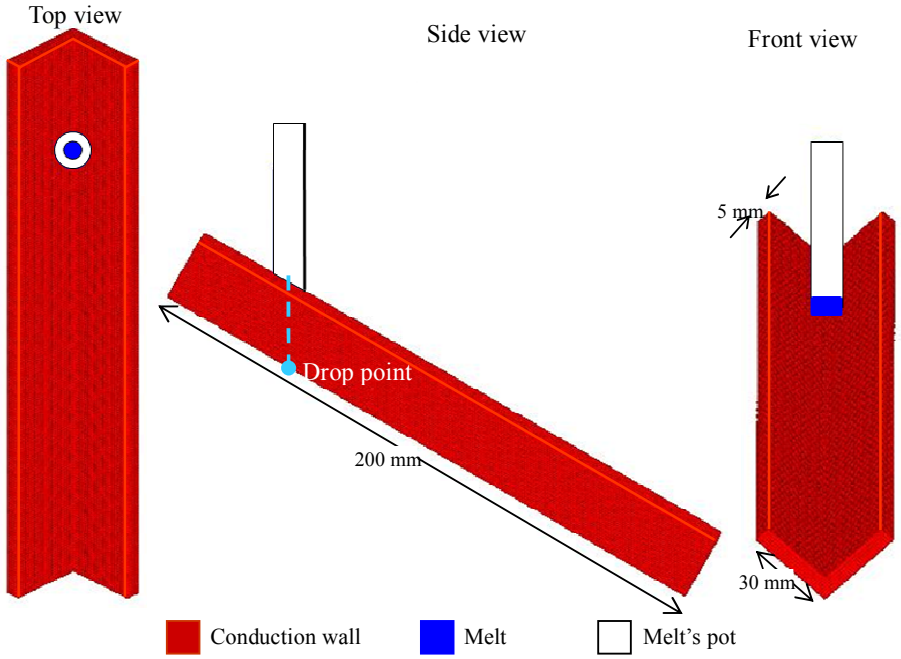

Fig. 3 Geometrical setup of simulation.

4. Simulation Results and Discussion

4. 1 Simulation Setup and Boundary Conditions

In the present 3D simulations, the initial particle distance Δl was set to 1 mm, and the time step size was 0.1 ms. **Figure 3** shows the channel geometry for the present simulations. The melt are represented by 800 – 1500 moving particles, depending on experimental conditions. The conduction wall is represented by an array of 200×30×5 moving particles corresponding to length, width and thickness, respectively. In the fluid dynamic calculation, only the first two layers of wall particles are used as boundary particles because the cut off radius r_e was chosen to be $2.1\Delta l$. In the heat conduction calculation, all wall particles are involved in simulating the heat transfer from the melt to the wall.

The boundary treatment in the fluid dynamics calculations are the zero Dirichlet for pressure and homogeneous Neumann condition for velocity divergences in determining pressure for particles on the free surface. For heat and mass transfer calculations, the Dirichlet boundary conditions are applied by setting the most outer wall layer temperature as air temperature.

To validate the fluid dynamic models for solidification behavior of melt flows on a cold structure wall, the measured transient penetration length and mass distribution of frozen molten metal are compared with simulation results. Here, the penetration length is defined as the length of the melt on the conduction wall as measured from the drop point. The mass distribution in the direction of the longitudinal length of the wall was measured for the four equal-length zones of the frozen melt. An example of the frozen melt and zone definition is presented in **Fig. 4**.

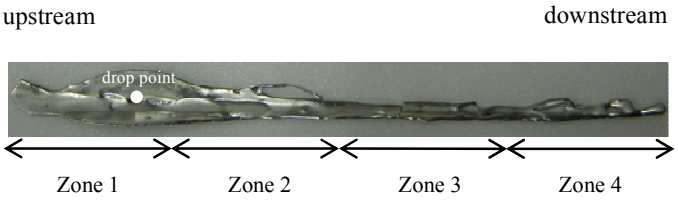

Fig. 4 An example of frozen melt and zone definition (Case C: copper wall, V_m=1.5 cm^3).

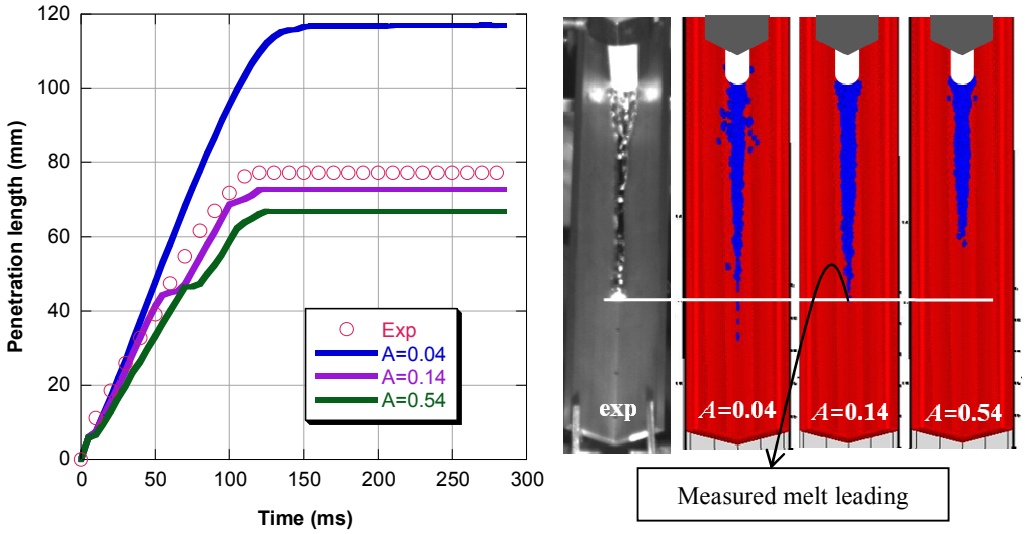

Fig. 5 Comparison of penetration between simulations using different rheology parameter A and experiment (Case A: copper wall, V_m = 1 cm^3).

4. 2 Rheology Parameter

To simulate the solidification behavior of the melt on the cold structure, it is necessary to determine the rheology parameter A appearing in Eqs. (26) and (27). Its optimization was performed by certain parametric calculations, labeled as Case A. **Figure 5** shows the simulation results of transient penetration length and frozen-melt shape with different rheology parameters in the range 0.04 – 0.54. In the simulation results, which are indicated by the left three images, the red and blue colors indicate the conduction wall and the melt, respectively. The white and grey colored parts, which represent the melt pot, are intentionally added to make visual comparisons easier. By

comparing the shape of frozen melt and the transient penetration length between experiment and simulation, we found $A = 0.14$ as a reasonable value for the rheology parameter.

Figure 6 shows visual comparisons of the solidification process between results of experiment and simulation using $A = 0.14$ for Case B. As can be seen in this figure, where the simulation results are presented on the left side for each instant of time, the simulation and experimental results indicate reasonable agreement in the shape of the melt during solidification onto the wall. The penetration lengths of melt measured in the experiment are also reasonably reproduced by the present simulation.

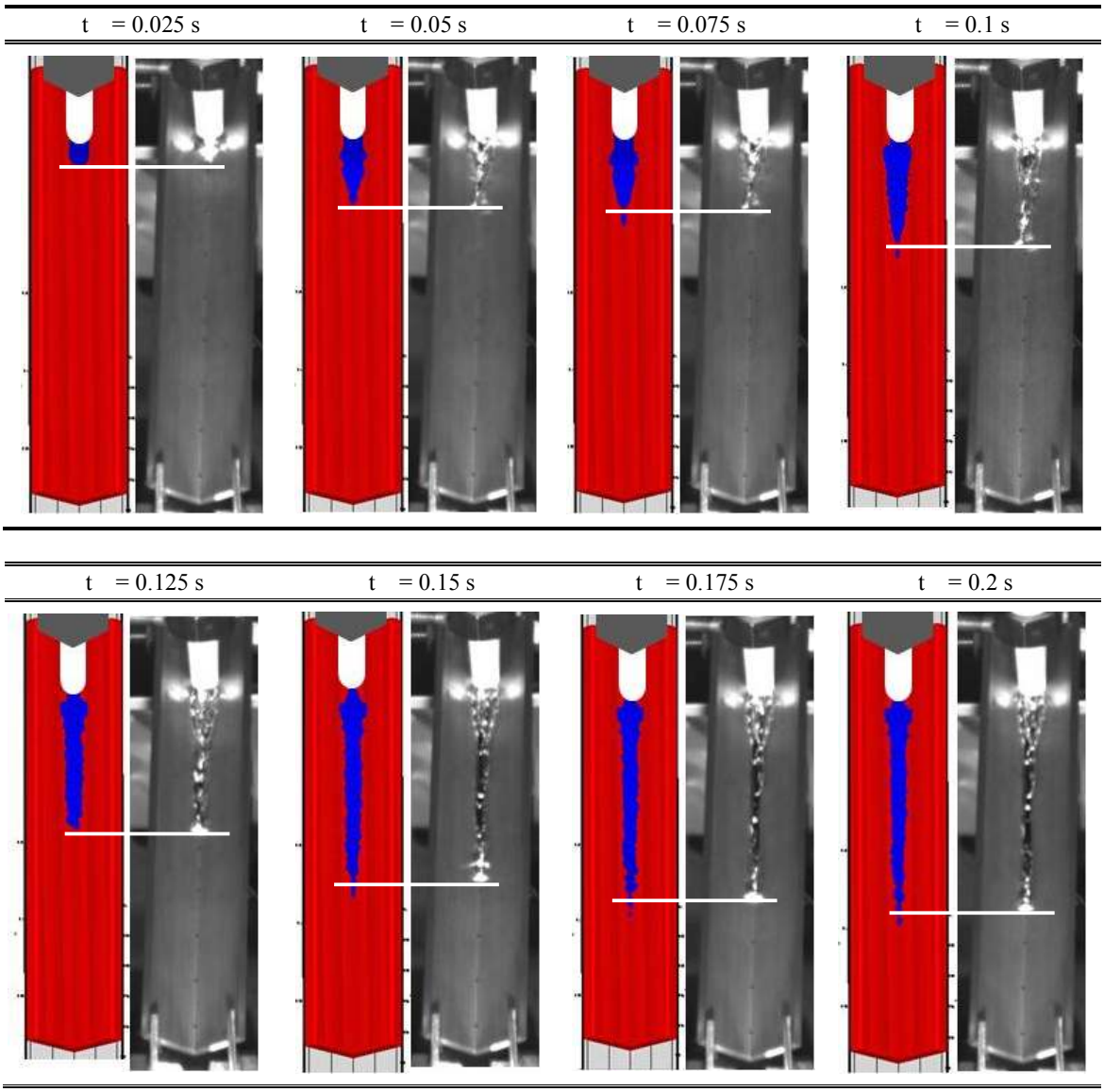

Fig. 6 Comparison of visualization results for transient solidification behavior between simulation and experiment (Case B: brass wall, $V_m = 1.5$ cm^3).

4. 3 Transient Penetration Length

Figure 7 shows the transient penetration length in Cases B and C. The simulation results for penetration behavior show fairly good agreements with experiment. In the initial stages, the transient

penetration length increases rapidly and then after a certain time the increase in penetration gradually reduces until the melt completely freezes (no change in the penetration length). The rapid increase in penetration length in the initial stage is due to melt impacting with the conduction wall. The initial velocity of melt in the pot is set to zero and is allowed to fall gravitationally. Given this impact velocity, melt penetration develops rapidly in the initial stages. However, as the melt reaches the wall, heat transfer from the hot melt to cold conduction wall occurs. Due to the rheological effect of the melt, the resulting temperature decrease leads to an increase in the viscosity force, which suppresses the melt velocity. The slower movement of the melt will lead to a smaller change in penetration length. When melt temperatures reach freezing point, melt viscosity becomes very large and the melt will completely stop penetrating the wall. For this reason, the heat and mass transfer model as well as the viscosity model play important roles in representing the transient behavior of melt penetration, which is reasonably reproduced by the present simulations. In addition, the simulation solidification time, *i.e.* the time taken for the melt to stop flowing in the wall agrees well with measurements.

In the simulation results, small changes of penetration length happened in the range 50 – 70 ms in Cases A (**Fig. 5**; A = 0.14) and C (**Fig. 7-b**) are resulted from the movement of melt's leading edge which is being overtaken by the following melt. When the leading edge begins to solidify, the change of penetration length becomes small (in the range 50 – 70 ms). The following melt, which flows above the previously solidified melt, will then overtake the leading edge so that the change of penetration length becomes large thereafter. The similar behavior was also observed occasionally in the experiments, although it cannot be seen in the experimental cases shown in **Figs. 5** and **7**.

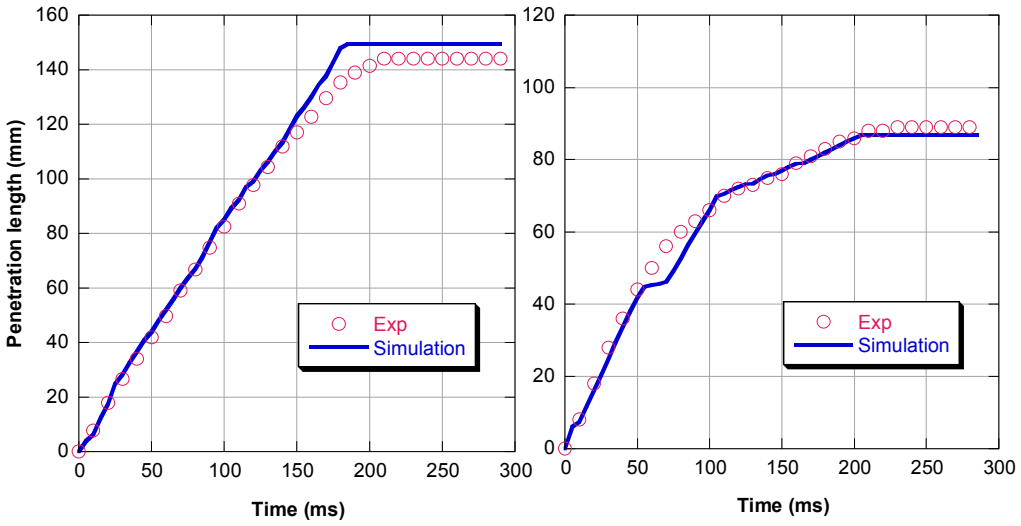

(a) Case B: brass wall, V_m = 1.5 cm^3 **(b) Case C: copper wall, V_m = 1.5 cm^3**

Fig. 7 Comparison of transient penetration length between simulation and experiment (Cases B and C).

4. 4 Melt Mass Distribution

The results of frozen-melt mass distribution in Cases A, B and C are shown in **Fig. 8**. As can be seen in Fig. 8, the comparison between experiments and simulations shows good quantitative agreement. All cases indicate the same tendency for the mass distribution. Much more of the melt freezes in Zones 1 and 2, while Zone 4 yields the smallest amount of frozen mass. Approximately 70 – 75 vol.% of the melt solidify in Zones 1 and 2 is due to the rapid heat transfer just after the melt

impact on the wall and the resultant viscosity change. The remaining melt will flow along the wall with slower velocity due to the viscosity increase.

For the copper wall cases (Cases A and C), Zone 1 has a higher mass than Zone 2, while for the brass wall case (Case B) Zone 2 has a higher mass than Zone 1. This is because the differences of the heat transfer rate to the wall (copper has 3.5 times larger thermal conductivity than brass). As soon as the melt reaches the wall, the melt will move both upwards and downwards direction. Due to the high thermal conductivity of copper, the melt that moves in the upward direction solidifies instantly in Zone 1. While for brass wall case, the melt solidification develops more slowly. Thus, the melt which once moves in upward direction will begin to flow downstream due to gravity without solidification and will eventually solidifies in Zone 2.

The present simulation results, especially for the different wall materials suggest that the fundamental models employed in the developed code reasonably represent heat transfer behavior from the molten melt to the wall under the present experimental conditions. This is because it dominates solidification behavior, which was characterized by the melt penetration length and the melt mass distribution.

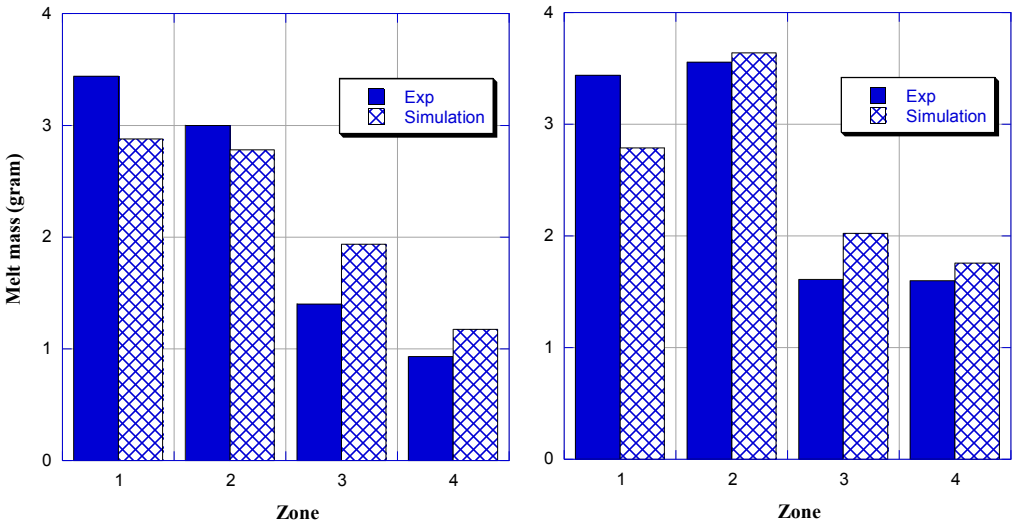

(a) Case A: copper wall, V_m = 1 cm^3 **(b) Case B: brass wall, V_m = 1.5 cm^3**

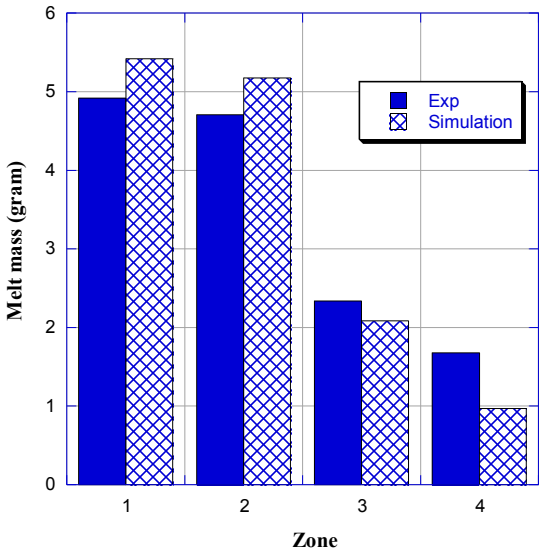

(c) Case C: copper wall, V_m = 1.5 cm^3

Fig. 8 Comparison of solidified-melt mass distribution (Cases A, B and C).

5. Concluding Remarks

A 3D computational code using the finite volume particle (FVP) method was developed to simulate solidification behavior of molten-metal flows on structure. The fundamental models employed to represent fluid-dynamics behaviors including melt rheology and heat and mass transfers were validated using a series of molten-metal solidification experiments. The comparison of penetration length and melt mass distribution between experiments and simulations shows good quantitative agreement under the present experimental conditions. The present verification results show applicability of the developed code to fundamental behavior of molten-metal flows with solidification. Further model verification would be necessary to demonstrate wide validly of the present computational framework based on the FVP method under various thermal and hydraulic conditions.

Acknowledgements

One of the authors, Rida SN Mahmudah acknowledges the support from the Ministry of Education, Culture, Sports, Science and Technology of Japan under the Monkagakusho scholarship. The computation was mainly performed using the computer facilities at the Research Institute for Information Technology, Kyushu University.

References

1) R. Wilson, Physics of Liquid Metal Fast Breeder Safety, Rev. Mod. Physics, Vol.4 (1977).
2) Sa. Kondo, K. Konishi, et al., Experimental Study on Simulated Molten Jet-coolant Interaction, Nucl. Eng. Des., Vol.204, pp. 377-389 (1995).

3) W. Peppler, A. Kaiser, et al., Freezing of a Thermite Melt Injected into an Annular Channel Experiments and Recalculations, Exp. Therm. Fluid Sci., Vol. 1, No. 1, pp. 335-346 (1988).
4) M. M. Rahman, Y. Ege, et al., Simulation of Molten Metal Freezing Behavior on to a Structure, Nucl. Eng. Des., Vol.238, pp.2706-2717 (2008).
5) M. K. Hossain, Y. Himuro, et al., Simulation of Molten Metal Penetration and Freezing Behavior in a Seven-pin Bundle Experiment, Nucl. Sci. Tech., Vol.46, No. 8, pp.799-808 (2009).
6) Sa. Kondo, Y. Tobita, et al., SIMMER-III: An Advanced Computer Program for LMFBR Severe Accident Analysis, Proc. Int. Conf. on Design and Safety of Advances Nuclear Power Plant (ANP'92), Tokyo, Japan, Oct. 25-29, 1992, IV, 40.5-1 (1992).
7) Y. Tobita, Sa. Kondo, et al,. Current Status and Application of SIMMER-III, An Advanced Computer Program for LMFR Safety Analysis, Proc. Second Japan-Korea Symposium on Nuclear Thermal Hydraulics and Safety (NTHAS2), Fukuoka, Japan, Oct. 15-18, 2000, 65 (2000).
8) J. Monaghan, Smoothed particle hydrodynamics, Rep. Prog. Phys., Vol.68, pp.1703–1759 (2005).
9) S. Koshizuka and Y. Oka, Moving-particle Semi-implicit Method for Fragmentation of Incompressible Fluid, Nucl. Sci.Eng, Vol.123, pp.421-434 (1996).
10) K.Yabushita and S. Hibi, A finite volume particle method for an incompressible fluid flow, Proc. Computational Engineering Conference, Vol.10, pp.419-421 (2005), [in Japanese]
11) S. Koshizuka, H. Ikeda, et al., Numerical Analysis of Fragmentation Mechanism in Vapor Explosions, Nucl. Eng. Des., Vol.189, pp.423-433 (1998).
12) S. Zhang, S. Kuwabara, et al., Simulation of Solid-fluid Mixture using Moving Particle Methods, J. Compt. Phys., Vol.228, pp.2552-2565 (2009).
13) S. Zhang, L. Guo, et al., Simulation of Single Bubble Rising Up in Stagnant Liquid Pool with Finite Volume Particle Method, Proc. of the Sixth Japan-Korea Symposium on Nuclear Thermal Hydraulics and Safety (NTHAS6), Okinawa, Japan, Nov. 24-27, 2008, N6P1022 (2008).
14) M. Kondo, K. Suzuki, et al., Surface Tension Model Using Inter-particle Force in Particle Method, FEDSM 2007 I Symposia (Part A), San Diego, USA, Jul. 30 – Aug. 2, 2007, pp. 93-98 (2007).
15) S. Zhang, K.Morita, et al., A New Algorithm for Surface Tension Model In Moving Particle Methods, Int. J. Numer. Meth. Fluids, Vol.55, pp.225-240 (2007).
16) F. Xiao, T. Yabe, et al., An Algorithm for Simulating Solid Objects Suspended in Stratified Flow, J. Compt. Phys Comm., Vol.102, pp.147-160 (1997).
17) L. Guo, S. Zhang, et al., Fundamental Validation of the Finite Volume Particle Method for 3D Sloshing Dynamics, Int. J. Numer. Meth. Fluids [in press].
18) K. Morita, T. Matsumoto, et al., Development of Multicomponent Vaporization/condensation Model for a Reactor Safety Analysis Code SIMMER-III: Theoretical Modeling and Basic Verification, Nucl. Eng. Des., Vol.220, pp.224-239 (2003).
19) L. Guo, Y. Kawano, et al., Numerical Simulation of Rheological Behavior in Melting Metal using Finite Volume Particle Method, J. Nucl. Sci. Tech, Vol.47, No.11, pp.1011-1022 (2010).
20) D. Thomas, Transport Characteristics of Suspensions, J. Colloid Sci., Vol.20, pp.267-277 (1965).